scientific reports

OPEN

Green synthesis of magnetite (Fe_3O_4) and hematite (Fe_2O_3) nanoparticles using *Moringa oleifera* and *Psidium guajava* leaf extracts for sustainable applications

Syeda Khurshida Begum[1]✉, Dalia Shabnam[1], Nazmul Haque[1], Mohammad Jahidul Alam[1], Jannatul Ferdous[1], Umme Juharia Binte Nur[1], Kaniz Fatema[1], Rayhana Jannat Shabiha[1], Ronald J. Clarke[2], Pial Chowdhury[3] & Md. Nizam Uddin[3]

Magnetite (Fe_3O_4) and hematite (Fe_2O_3) nanoparticles hold significant potential for catalysis, environmental remediation, biomedicine, and energy generation. However, conventional synthesis methods for iron-oxide nanoparticles (IONPs) are often complicated or involve hazardous reagents, limiting scalability. Although plant extract-mediated green synthesis offers better alternatives, many rely on rare or expensive biomaterials and hazardous precursors or pH-adjusting chemicals, compromising eco-friendliness and cost-effectiveness. To address these challenges, we developed a truly green, efficient, and economical protocol for synthesizing the nanoparticles smaller than 50 nm. Widely available *Moringa oleifera* (Moringa) and *Psidium guajava* (Guava) leaf extracts, along with a relatively low-cost, non-toxic $FeSO_4 \cdot 7\ H_2O$ precursor at an optimized concentration, were employed without any harmful chemicals for pH adjustment. Additionally, a unique calcination strategy was applied. This method produced nanoparticles with an average size of 20–30 nm, confirmed by Field Emission Scanning Electron Microscopy (FESEM). Crystalline structures of the magnetite and hematite nanoparticles were validated by X-Ray Diffraction (XRD), and Fe–O bonding with organic capping was identified by Fourier Transform Infrared Spectroscopy (FTIR). These nanoparticles exhibited superparamagnetic behavior with saturation magnetization of 6–13 emu/g, measured by Vibrating Sample Magnetometry (VSM), and strong optical absorption with band gaps from 1.52 to 4.78 eV, determined by UV-Vis spectroscopy and Tauc's plots. Preliminary antibacterial and photocatalytic tests showed moderate bioactivity, highlighting potential environmental and biomedical uses. This eco-friendly, scalable approach combines abundant natural extracts and avoids the use of harmful chemicals, advancing sustainable production of magnetite and hematite nanoparticles and addressing a critical gap in green nanotechnology.

Keywords Green synthesis, *Moringa oleifera*, *Psidium guajava*, Superparamagnetic, Magnetite, Hematite, Nanoparticle, Sustainable applications

Nanoparticles exhibit unique physicochemical properties due to their high surface area-to-volume ratio and quantum confinement effects, resulting in exceptional catalytic, magnetic, electronic, and optical properties[1,2]. These distinctive features have enabled nanomaterials to significantly improve the performance of various energy generation systems, including photovoltaics, lithium-ion batteries, and fuel cells[3–5]. Beyond energy applications, nanoparticles have shown immense promise in biomedical fields[6] and environmental remediation technologies[7].

[1]Energy, Environment and Bio-Nanotechnology Group (EEBN Group), Professor M A Saleh Research Laboratory, Department of Chemistry, University of Chittagong, Chittagong 4331, Bangladesh. [2]School of Chemistry, University of Sydney, Camperdown, NSW 2006, Australia. [3]Department of Chemistry, Shahjalal University of Science and Technology, Sylhet 3114, Bangladesh. ✉email: skbegum@cu.ac.bd

Among various metal and metal oxide nanoparticles, iron oxide nanoparticles (IONPs) stand out due to their multifunctionality and broad range of applications[8,9]. They possess excellent magnetic properties, chemical stability, and biocompatibility[10,11]. These nanoparticles play important roles in fields such as catalysis[12], data storage[13], electronics[14,15], imaging[16], biosensing[17] and water treatment[18]. Their biomedical applications are particularly diverse, including cancer therapy[19], drug delivery[20], hyperthermia treatment[21], and antimicrobial applications[22]. Additionally, magnetite and hematite nanoparticles are highly efficient magnetic nano adsorbents for removing toxic heavy metals such as arsenic, chromium, cadmium, and lead from contaminated water[23]. Their photocatalytic and antibacterial properties further highlight their potential in energy generation and their use as alternatives to conventional antibiotics[24,25].

Various methods are available for the synthesis of iron oxide nanoparticles[26,27]; however, many of the common approaches have notable limitations. Physical methods such as chemical vapor deposition and laser pyrolysis are often expensive and complex[27,28], whereas chemical reduction approaches usually involve toxic reagents, raising environmental and safety concerns[29,30]. These limitations have spurred growing interest in green synthesis routes that are sustainable and cost-effective[31–33]. Among green synthesis techniques, plant-mediated approaches offer advantages over microbial methods, including simpler protocols and greater scalability[34–42]. Various plant parts from species such as *Lagenaria siceraria*, *Hibiscus rosa-sinensis*, and *Avicennia marina* have been used in synthesizing iron oxide nanoparticles[36–42]. The phytochemicals present in plant extracts, including polysaccharides, vitamins, amino acids, proteins, saponins, alkaloids, terpenes, phenolics, flavonoids, and enzymes, serve as both reducing and stabilizing agents[43–52]. These biomolecules facilitate the reduction of metal ions to nanoparticles and simultaneously cap the particles, controlling their size at the nanometer sca le[43,44,47,53,54]. Previous studies have also revealed that the nature of the plant extract strongly influences the size and morphology of the produced nanoparticles[43,46,47,53,54].

Despite promising progress, several challenges remain in the green synthesis of iron oxide nanoparticles. These include: (1) insufficient characterization to confirm the formation of targeted nanoparticles with sizes below 100 nm[51,55,56]; (2) dependence on pH-adjusting chemicals which compromise the “green” aspect of the process[52,57–59]; (3) reliance on rare or expensive plant sources[52,55,57–61]; and (4) use of hazardous iron precursors such as $FeCl_3$ or $Fe(NO_3)_3$, which pose environmental risks[52,57–62].

Considering the limitations of existing synthesis methods, we propose an optimized green protocol to synthesize well-defined magnetite and hematite nanoparticles under 50 nm in size, using widely available *Moringa oleifera* (Moringa) and *Psidium guajava* (Guava) leaf extracts, as eco-friendly reducing and capping agents, combined with a safe and cost-effective iron precursor $FeSO_4{\cdot}7\ H_2O$. This method eliminates the need for hazardous chemicals for pH adjustment and incorporates a novel calcination step, enabling a scalable and environmentally sustainable route for synthesis of the targeted nanoparticles. The use of two distinct plant extracts under identical synthesis conditions provides insights into how the choice of biological agent can influence nanoparticle morphology and functional properties, with preliminary evaluations, which indicate differences in photocatalytic and antibacterial performance. This study thus lays the foundation for advancing the sustainable production of magnetite and hematite nanomaterials for diverse technological applications.

Materials and methods

Materials

Freshly prepared extracts from Moringa and Guava leaves were used in this study. Commercial iron sulfate heptahydrate ($FeSO_4{\cdot}7H_2O$) with a purity of 98.5%, obtained from Merck, Germany, served as the precursor salt. Instruments used include a digital balance (AND, FR-200, 210 × 0.0001 g, Shimadzu, Japan), a muffle furnace (ISYZU SEISARYSHO CO., LTD), a pH meter (HANNA instruments, pH 210, Microprocessor pH meter), and a magnetic stirrer (Eyela, Japan).

Preparation of plant leaf extracts

Fresh Moringa and Guava leaves were collected from local trees in Chittagong. The leaves were thoroughly washed and dried at room temperature for approximately 24 h. About 200 g of each dried leaf type was chopped into small pieces and boiled separately in 1 L of distilled water. After boiling, the mixtures were strained, cooled, and allowed to settle. The clear top-layer extracts were collected and stored in a refrigerator. The Moringa leaf extract appeared faint yellowish-brown, while the Guava leaf extract was bright reddish-brown. The pH values of the freshly prepared extracts were measured as 5.1 for Moringa and 5.7 for Guava.

Synthesis of iron oxide nanoparticles

Iron oxide nanoparticles (IONPs) were synthesized separately using Moringa and Guava leaf extracts. 500 mL of 0.05 M $FeSO_4{\cdot}7H_2O$ solution with a pH of 3.1 was prepared and 250mL of it was placed in a 500 mL beaker on a magnetic stirrer. While stirring, approximately 180 mL of Moringa leaf extract was added dropwise from a burette to control nucleation and growth. After complete addition, the solution turned greenish-brown and the pH increased to 3.5. The reaction mixture was left undisturbed at room temperature for 24 h to allow reduction and particle maturation. The resulting slurry-like precipitate was collected, washed three times with distilled water, dried in a Petri dish at 100 °C for 1 h, ground to a fine powder, and reheated for 2 h. The powder was then calcined in a muffle furnace at 300 °C for 3 h. and subsequently at 600 °C for 3 h. An identical procedure was followed using Guava leaf extract with another 250 mL of the $FeSO_4{\cdot}7H_2O$ solution. In this case, the mixture turned deep black after mixing and the pH was recorded as 3.8. The synthesis route has been presented in Fig. 1.

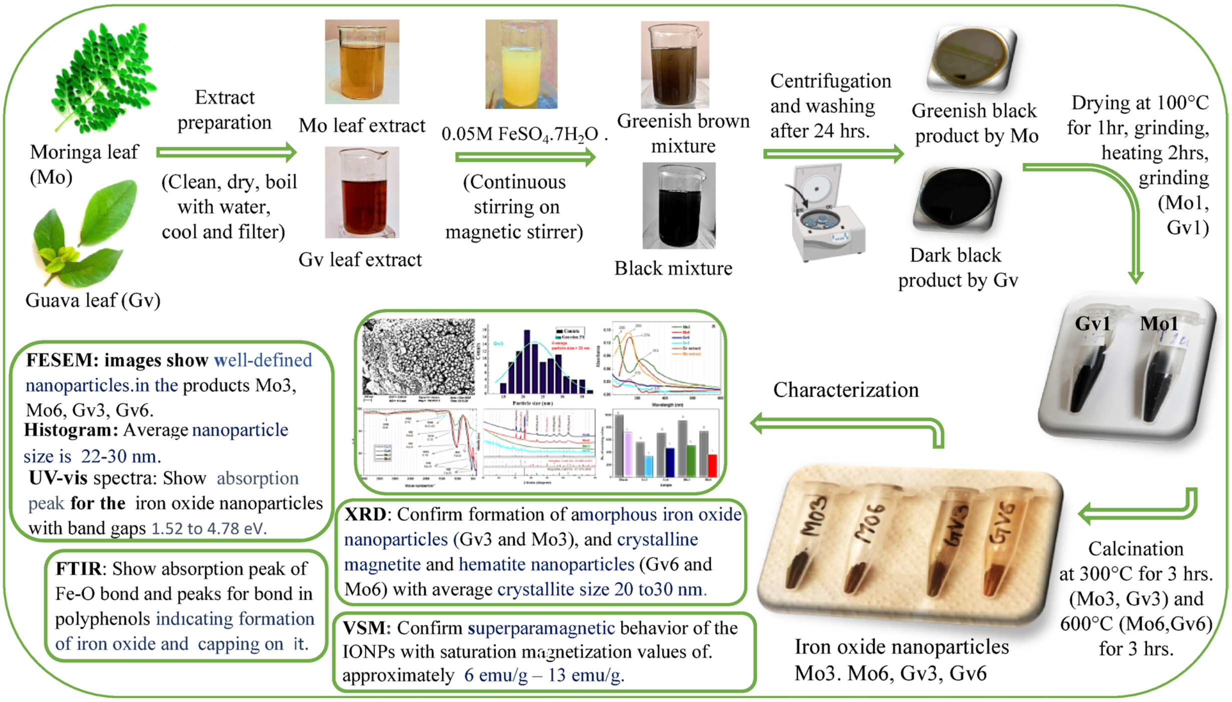

Fig. 1. Synthesis route for well-defined iron oxide nanoparticles (magnetite and hematite) using Moringa (Mo) and Guava (Gv) leaf extracts.

Results and discussion

Visual observations and initial color changes

The immediate color changes observed upon adding Moringa or Guava leaf extracts to the ferrous sulfate solution may indicate the reduction of iron ions and the formation of nanoparticles. During the synthesis process, subsequent thermal treatments including drying at 100 °C and calcination at 300 °C and 600 °C induced further distinct color changes as presented in Fig. 1. These color variations suggest modifications in the physicochemical properties of the synthesized nanoparticles, potentially including changes in particle size, morphology, and crystalline structure,

Formation of iron/iron hydroxide nanoparticles

Depending on the diverse bioactive molecules present in the Moringa and Guava leaf extracts[43,46,48,63,64] iron or iron-hydroxide nanoparticles are formed in the solution mixture. Moringa leaf extract contains molecules such as epicatechin, ferulic acid, ascorbic acid, kaempferol, quercetin, and chlorogenic acid[45,65–67], whereas Guava leaf extract is rich in ascorbic acid, kaempferol, quercetin, gallic acid, apigenin, luteolin, and myricetin[68–70]. The chemical structures of these key compounds are illustrated in Fig. 2a. These biomolecules reduce Fe^{2+} ions from ferrous sulphate solution by electron transfer from their hydroxyl (-OH) groups, converting iron ions into elemental iron species[64]. Simultaneously, they adsorb onto the nanoparticle surfaces, effectively capping them to prevent aggregation and maintain nanoscale size. However, the acidic environment of the plant extracts and their mixtures with iron precursor solutions ($pH < 7$) promotes in situ oxidation of the freshly formed iron nanoparticles, converting them into iron hydroxides. This proposed mechanism aligns with experimental evidence reported by Abdullah et al.[52], linking acidic conditions to iron hydroxide formation. Here, variations in the phytochemical composition of the plant leaf extracts might affect the characteristics of the synthesized nanoparticles[44,47,53,64].

Formation of magnetite and hematite nanoparticles

Upon calcination at 300 °C and subsequently at 600 °C, FeO is likely formed initially through dehydration reactions. Due to the thermodynamic instability of FeO, higher temperatures induce its transformation into both amorphous and crystalline iron oxide phases, such as magnetite (Fe_3O_4) and hematite (Fe_2O_3), consistent with previous reports on the thermal behavior and phase transformations of iron oxides[71]. For convenience, iron oxide nanoparticles synthesized using Moringa leaf extract are labeled as Mo3 when calcined at 300 °C and Mo6 when calcined at 600 °C. Similarly, nanoparticles synthesized using Guava leaf extract are designated as Gv3 and Gv6 when calcined at 300 °C and 600 °C, respectively. A detailed schematic of the proposed mechanism is shown in Fig. 2b.

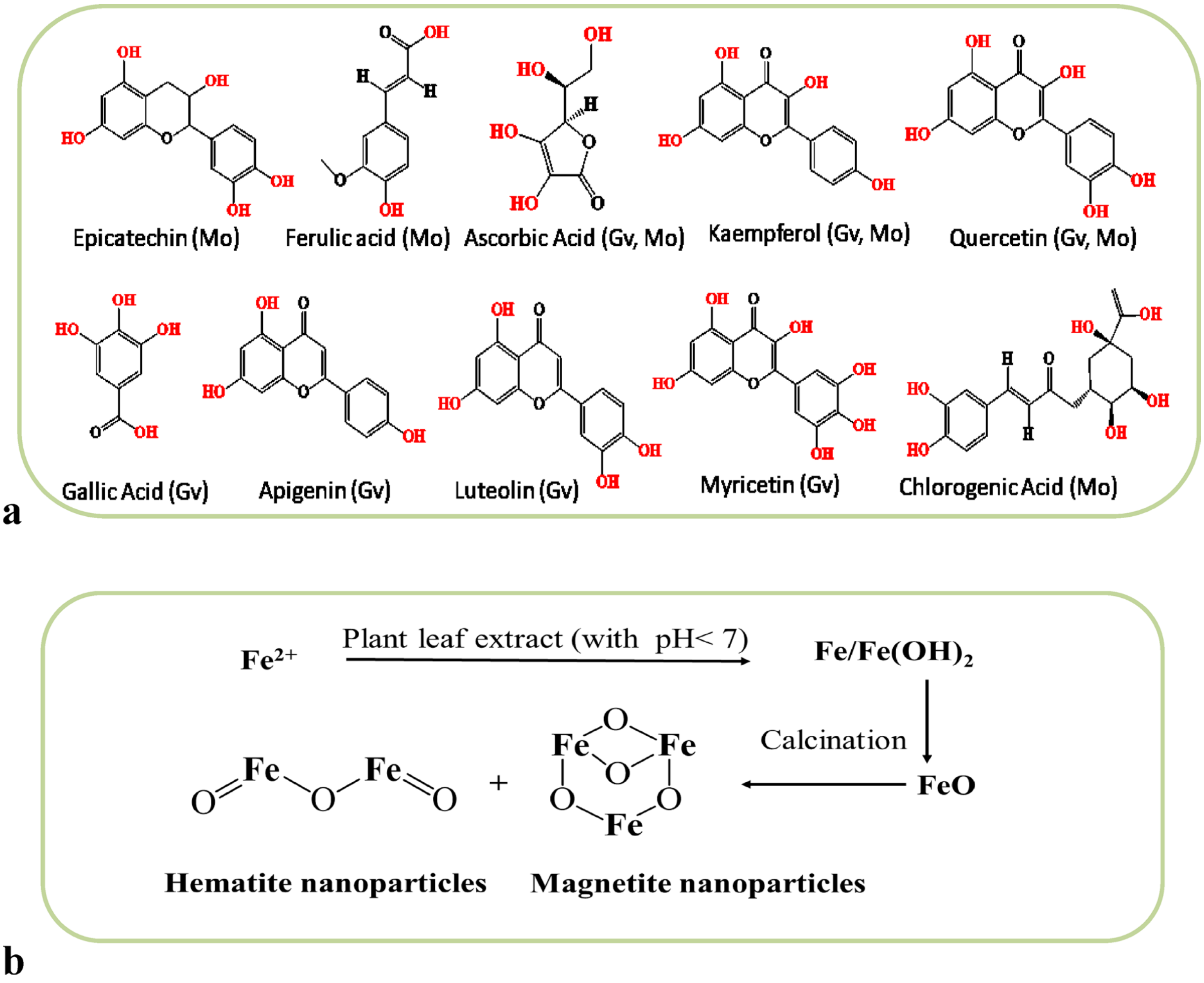

Fig. 2. **a**) Different phenolic components present in Guava (Gv) and Moringa (Mo) leaf extracts and **b**) mechanism of formation of iron oxide nanoparticles (magnetite and hematite) by the extract components from ferrous sulphate solution.

Analysis of the synthesized nanoparticles

To verify the successful synthesis of the targeted iron oxide nanoparticles (IONPs) and thoroughly evaluate their size, morphology, crystalline phase, magnetic properties, presence of metal–oxygen bond, and surface coating, the synthesized products were subjected to a comprehensive set of characterization techniques. These techniques included Field Emission Scanning Electron Microscopy (FESEM), X-ray Diffraction Spectroscopy (XRD), Ultraviolet-Visible Spectroscopy (UV-Vis), Fourier Transform Infrared Spectroscopy (FTIR), and Vibrating Sample Magnetometry (VSM). The results obtained from these analyses are discussed in detail below.

Field emission scanning electron microscopy (FESEM) analysis

The size and morphology of the nanoparticles were characterized by field emission scanning electron microscopy (FESEM) using a Sigma 300 model (Carl Zeiss, Germany). Figure 3a and b show FESEM micrographs of iron oxide nanoparticles synthesized using guava leaf extract and calcined at 300 °C (Gv3) and 600 °C (Gv6), respectively, at a magnification of 150,000×. The corresponding particle size distribution histograms are presented in Fig. 3c and d. The images reveal well-defined nanoparticles with sizes of below 100 nm. Size distribution analysis indicates average particle sizes of approximately 23 nm for Gv3 and 29 nm for Gv6. Similarly, Fig. 4a and b show FESEM images of iron oxide nanoparticles synthesized using moringa leaf extract calcined at 300 °C (Mo3) and 600 °C (Mo6), respectively. Their corresponding particle size distributions are shown in Fig. 4c and d. The Mo3 sample exhibits particle sizes ranging from approximately 15 to 40 nm, with an average size of 22 nm, whereas Mo6 shows a slight increase in average particle size to 30 nm. No significant morphological differences were observed between the samples. Overall, FESEM analysis confirms the successful synthesis of well-defined, nanosized particles by this synthesis approach. The nanoparticles exhibit narrow size distributions, with average diameters of approximately 22–23 nm for samples calcined at 300 °C and 29–30 nm for those calcined at 600 °C, aligning well with the desired size range for potential applications.

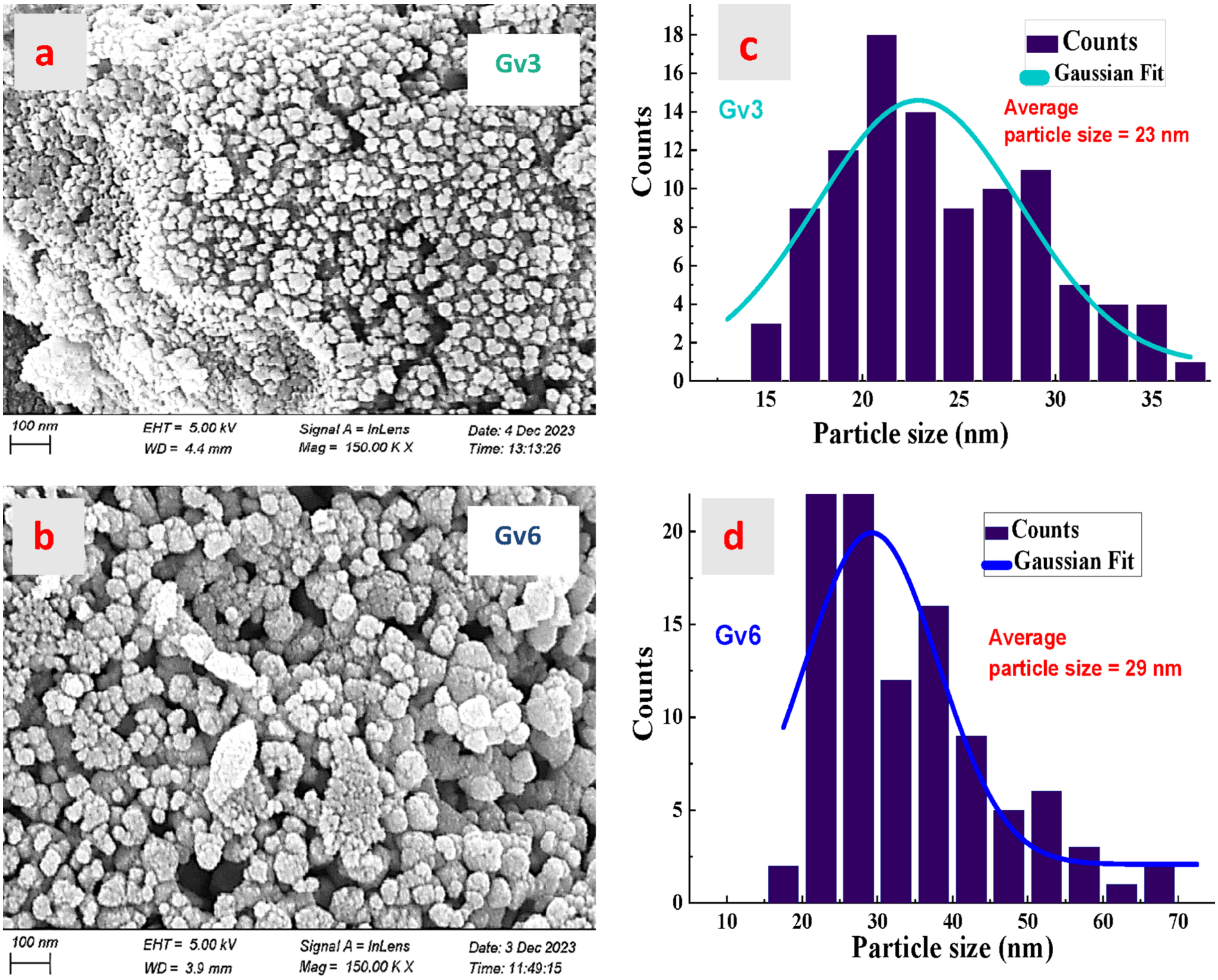

Fig. 3. FESEM images (**a**, **b**) and particle size distribution histograms (**c**, **d**) of iron oxide nanoparticles (magnetite and hematite) synthesized using Guava leaf extract and calcined at 300 °C (Gv3) and 600 °C (Gv6).

X-Ray diffraction (XRD) analysis

X-ray diffraction (XRD) analysis was performed to determine the crystallinity and phase composition of the synthesized iron oxide nanoparticles, as well as to gain detailed insights into their molecular and crystal structures. The analysis was conducted using a Rigaku SmartLab II diffractometer, which also enabled particle size estimation. Figure 5 displays the XRD patterns of nanoparticles synthesized via green synthesis using Moringa and Guava leaf extracts, calcined at 300 °C (Mo3, Gv3) and 600 °C (Mo6, Gv6).

For samples calcined at 600 °C (Mo6 and Gv6), diffraction peaks characteristic of crystalline magnetite and hematite phases were clearly observed. Specifically, Mo6 exhibited distinct reflections at 2θ values of 30.33°, 35.73°, 43.43°, 53.90°, 57.46°, and 63.11°, corresponding to the (220), (311), (400), (422), (511), and (440) planes, respectively, confirming magnetite formation at this temperature. The Mo3 sample calcined at 300 °C showed no prominent diffraction peaks, indicating an amorphous structure.

Similarly, Gv6 showed peaks at 2θ = 30.36°, 35.76°, 43.47°, 53.94°, 57.51°, and 63.16°, matching the same crystallographic planes as Mo6 and confirming a cubic magnetite structure. These patterns correspond well with the JCPDS standard cards for magnetite (Card No. 01-076-2949)[72] and also exhibit two prominent peaks attributable to hematite (Card No. 01-089-8103)[73], indicating predominantly magnetite with a minor hematite phase at 600 °C. The Gv3 sample calcined at 300 °C was mostly amorphous, though two weak magnetite peaks suggest the presence of a small crystalline fraction.

Crystallite sizes (D) were calculated using the Scherrer equation, ($D = k\lambda/B \cos\Theta$) implemented in the SmartLab Studio-II software. Here, k is Scherrer's constant (0.9), λ is the X-ray wavelength (1.54060 Å), B is the full width at half-maximum of the nanoparticle (3 1 1) plane, and Θ is the diffraction angle. The average crystallite sizes for Mo6 and Gv6 were found to be 30.4 nm and 28.2 nm, respectively. Interplanar d-spacing values were calculated as 2.51 Å for Mo6 and 2.50 Å for Gv6, indicating excellent lattice periodicity. The lattice parameters for magnetite were found as $a = b = c = 8.32687$Å for Mo6 and $a = b = c = 8.32045$ Å for Gv6, both closely matching the standard value of 8.34000 Å[73].

Hence, XRD analysis confirms the successful green synthesis of magnetite and hematite nanoparticles with temperature-dependent crystallization behavior: an amorphous structure predominates at 300 °C, whereas a

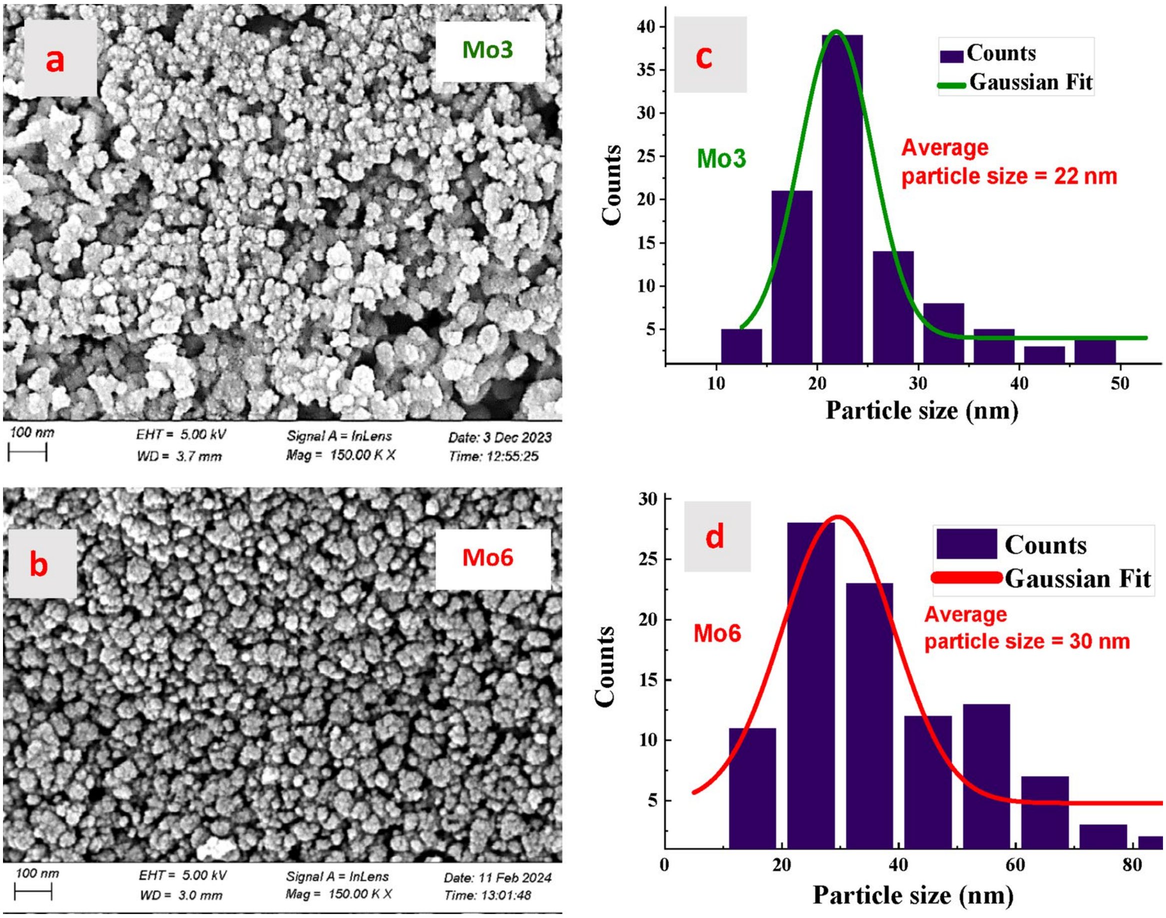

Fig. 4. FESEM images (**a**, **b**) and particle size distribution histograms (**c**, **d**) of iron oxide nanoparticles (magnetite and hematite) synthesized using Moringa leaf extract and calcined at 300 °C (Mo3) and 600 °C (Mo6).

mainly crystalline magnetite phase with minor hematite content forms at 600 °C. This demonstrates the efficacy of this synthesis approach combined with calcination temperature control for tailoring the phase and crystallinity of iron oxide nanoparticle.

UV-Visible absorption spectroscopy (UV-vis) analysis

UV-visible absorption spectroscopy was used to characterize the optical properties and identify photocatalytically active components within the synthesized iron oxide nanoparticles (Gv3, Gv6, Mo3, Mo6). Aqueous dispersions of the nanoparticles, prepared via sonication, were analyzed using a Shimadzu UV-1800 spectrophotometer. Figure 6a displays the spectra, including the UV-Vis spectra of moringa and guava leaf extracts obtained in the present study. The observed absorption spectra provided critical insights into the optical properties and nanoscale characteristics of the synthesized nanoparticles. Notably, the nanoparticles exhibited distinctive absorption peaks around 300 nm, consistent with their nanoscale dimensions as reported in previous studies[74–76]. Specifically, Mo3 (calcined at 300 °C in Moringa-mediated synthesis) demonstrated a broad absorption band spanning 300–400 nm, with a pronounced maximum at 315 nm, accompanied by a distinct high-energy peak at 230 nm. In contrast, the pure Moringa extract displayed a singular phenolic/chromophoric absorption feature at 268 nm, supporting the characteristic signature previously documented by Mohammed et al.[77] for this plant extract. Comparative analysis, referencing the data reported by Akbar et al.[76]., enabled the assignment of the absorption peak at 230 nm to hematite, while the peak at 315 nm was attributed to magnetite. For Mo6 (calcined at 600 °C), the absorption spectrum exhibited two distinct peaks at 272 nm and 333 nm, consistent with XRD evidence indicating phase transformation. In contrast, Guava-derived nanoparticles displayed markedly different optical characteristics. Gv3 (calcined at 300 °C) presented weakly resolved doublet features at approximately 300 nm and 335 nm, reflecting its mixed crystalline-amorphous structure. Furthermore, Gv6 showed a pronounced attenuation in absorption intensity, which contrasts sharply with the strong chromophoric peak at 274 nm observed in the native Guava extract[78]. The observed absorption peaks result from the characteristic surface plasmon resonance of the nanoparticles[79].

The band gaps of iron oxide nanoparticles Mo3 and Mo6, which displayed sharp absorption peaks, were calculated using absorbance data and Tauc plots following Tauc's equation $(\alpha h\nu)1/n = B(h\nu - Eg)$, where α represents the absorption coefficient, h is Planck's constant, ν denotes the photon frequency, Eg is the band gap

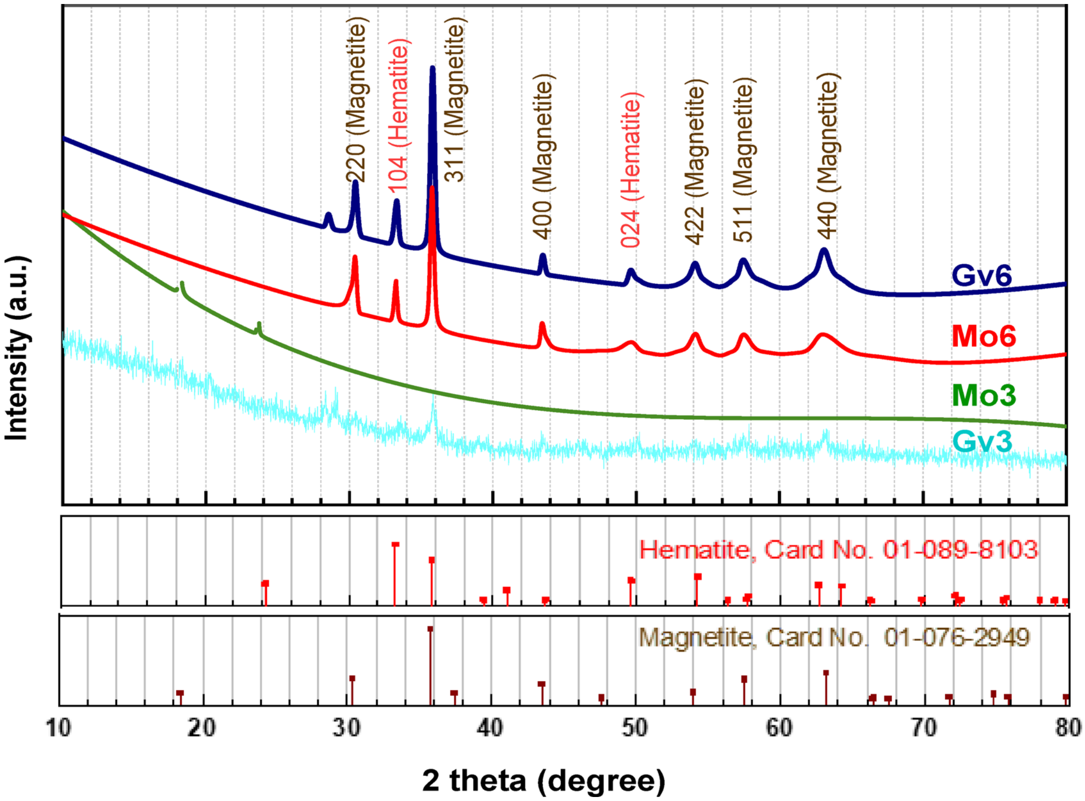

Fig. 5. XRD patterns of iron oxide nanoparticles (magnetite and hematite) synthesized using Guava (Gv) and Moringa (Mo) leaf extracts, calcined at 300 °C (Gv3, Mo3) and 600 °C (Gv6, Mo6). Reference patterns for magnetite[72] and hematite[73] are included for comparison.

energy, and B is a constant. The linear portion of the $(\alpha h\nu)^{1/2}$ versus $h\nu$ plot was extrapolated to intersect the energy axis, from which the band gap energy values were determined[77,80], as presented in Fig. 6b and c.

For Mo3, absorption at 315 nm, attributed to magnetite[76], corresponds to a band gap E_{g1}=1.52 eV while absorption at 230 nm, assigned to hematite[76], gives E_{g2}=3.91 eV. In the case of Mo6, absorption at 333 nm results in E_{g3}=3.73 eV, and at 272 nm, the band gap is E_{g4}=4.78 eV. The band gap values for the synthesized magnetite nanoparticles are consistent with the previously reported value of 4.5 eV by Hosseini et al.[81] although Akbar et al.[76]. reported lower band gaps of 2.22 eV for magnetite and 2.66 eV for hematite. While the band gap energy values of the synthesized IONPs indicate their photocatalytic activity, the band gap energy of 1.52 eV, observed for the Moringa-mediated nanoparticles calcined at 300 °C, falls within the visible light region. This value suggests highly efficient photon absorption through electron transitions from the valence band to the conduction band, highlighting the strong potential of these nanoparticles for photocatalytic activity which might be an indication of more efficiency of Moringa leaf extracts in getting photocatalytic iron oxide nanoparticles than of Guava leaf extract.

Overall, IONPs synthesized using Moringa and Guava leaf extracts exhibited distinct UV-Vis absorption patterns indicative of their nanoscale size and related to their phase composition. Moringa-derived nanoparticles showed strong absorption peaks and a lower band gap, indicating enhanced visible-light photocatalytic activity, whereas Guava-derived nanoparticles displayed weaker absorption and reduced photocatalytic potential. Both calcination temperature and plant extract type significantly influenced the optical and structural properties of the nanoparticles[47,64].

Fourier transform infrared spectroscopy (FTIR) analysis

The synthesized products (Gv3, Gv6, Mo3, and Mo6) were analyzed by Fourier-transform infrared (FTIR) spectroscopy to confirm the presence of Fe–O bonds in the products, identify whether iron oxides or iron hydroxides were formed, and detect the presence of capping agents originating from plant extracts. The recorded FTIR spectra are presented in Fig. 7. Distinct absorption bands observed at approximately 428, 464, 502, 546, and 592 cm^{-1} clearly indicate the presence of Fe–O bonds[82]. These spectral features fall within the characteristic region for metal–oxygen stretching vibrations, as extensively documented in the literature. For instance, Srivastava et al.[83] and Nag et al.[84] reported FTIR peaks at 562 cm^{-1} and 456 cm^{-1}, which were attributed to metal–oxygen stretching modes corresponding to Fe_3O_4 and α-Fe_2O_3, thereby confirming the formation of Fe_3O_4/α-Fe_2O_3 nanocomposites. The similarity of our observed peaks to these references supports the formation of analogous iron oxide phases in the present study.

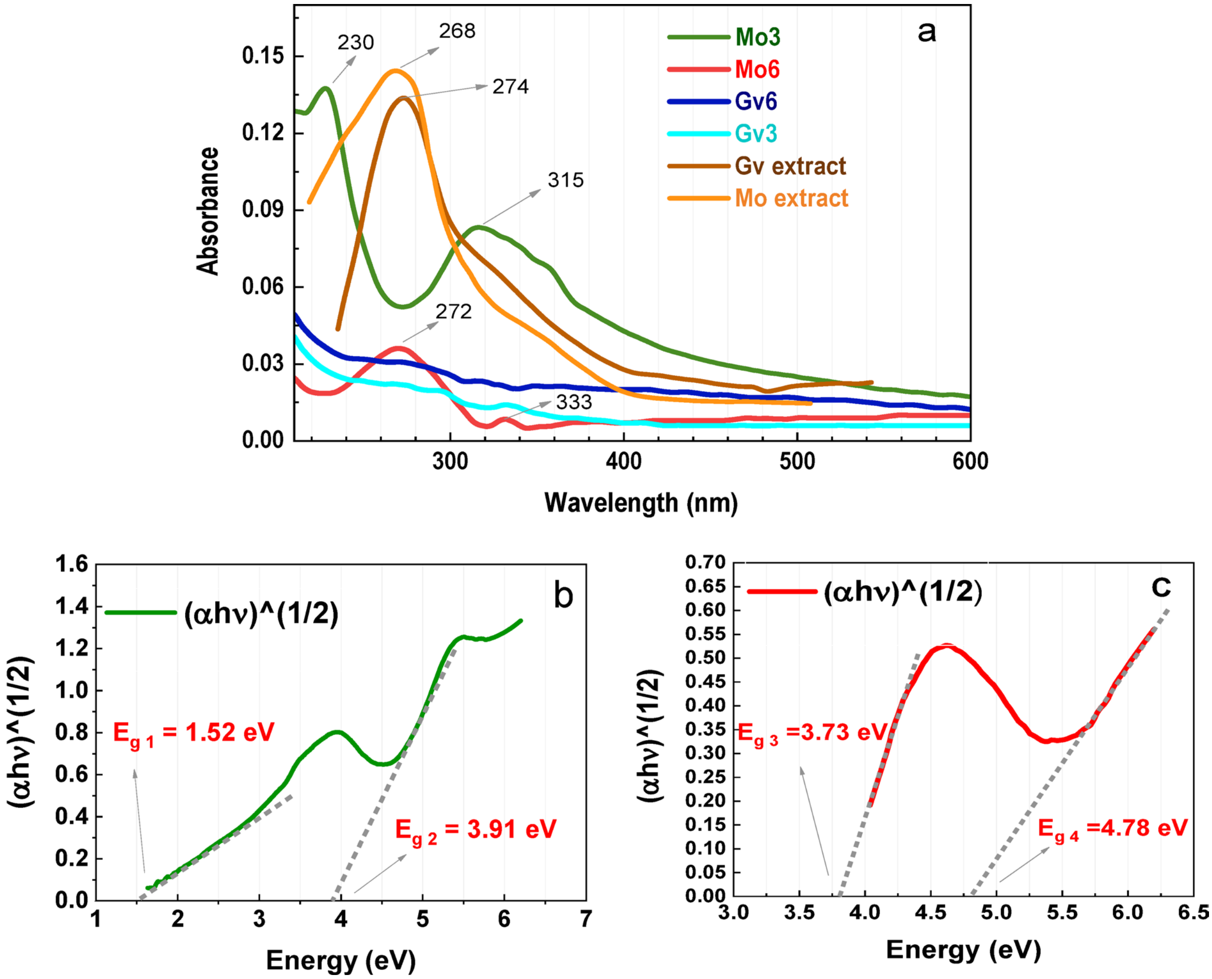

Fig. 6. UV-Vis absorption spectra of (**a**) Moringa leaf extract (Mo), Guava leaf extract (Gv), and iron oxide nanoparticles (magnetite and hematite) synthesized from these extracts and calcined at 300 °C (Mo3, Gv3) and 600 °C (Mo6, Gv6); (**b**) Tauc's plot for the Mo3 nanoparticles; and (**c**) Tauc's plot for the Mo6 nanoparticles.

Absorption bands appearing above 1000 cm^{-1} are typically associated with organic stabilizing or capping agents derived from phytochemicals present in the plant extracts[84,85]. In the spectra of Gv3 and Mo3, a broad and prominent peak at 3288 cm^{-1} corresponds to the stretching vibrations of hydroxyl (–OH) groups[86], which may originate from phenolic compounds inherent to the extracts or from residual iron hydroxide species. Notably, the intensity of these hydroxyl peaks decreases in the products calcined at 600 °C (Gv6 and Mo6), indicating a conversion of remaining iron hydroxide to iron oxide at the elevated calcination temperature. Additional absorption bands for Gv3 and Mo3 observed at 1016 and 1130 cm^{-1} can be assigned to C–O stretching[86,87], 1390 cm^{-1} to O–C = O asymmetric stretching[88], and 1584 cm^{-1} to C = C aromatic ring vibrations[89]. These are consistent with the presence of polyphenolic compounds acting as capping agents, as reported by Kumar et al.[85]., who identified FTIR peaks around 1100–1150 cm^{-1} (C–O stretching), 1380–1400 cm^{-1} (O–C = O asymmetric stretching), and 1580–1600 cm^{-1} (aromatic C = C stretching) as characteristic signatures of polyphenolic compounds involved in capping or stabilizing nanoparticles during synthesis. Furthermore, a distinct C–O stretching peak at 1016 cm^{-1} was also detected, likely originating from polyphenols in the plant extracts. Upon calcination at 600 °C, the intensity of most of these organic-related peaks decreases, except for the C–O stretching band, which remarkably intensifies. This phenomenon aligns with previous reports[84,85] where thermal treatment led to the enhancement of certain C–O absorption bands, possibly due to structural rearrangements of the organic moieties.

In summary, the FTIR spectra confirm the formation of iron oxide nanoparticles through the presence of characteristic Fe–O vibrational bands while also revealing the transformation of iron hydroxides to oxides upon calcination. Simultaneously, distinct absorption features attributable to biomolecular functional groups validate the effective capping and stabilization of the nanoparticles by phytochemicals from the plant extracts.

Vibrating sample magnetometry (VSM) analysis

The magnetic properties of the synthesized IONPs were studied using a Vibrating sample magnetometer (VSM) at room temperature. The VSM graphs for Mo6 and Gv6 nanoparticles, shown in Fig. 8, exhibit

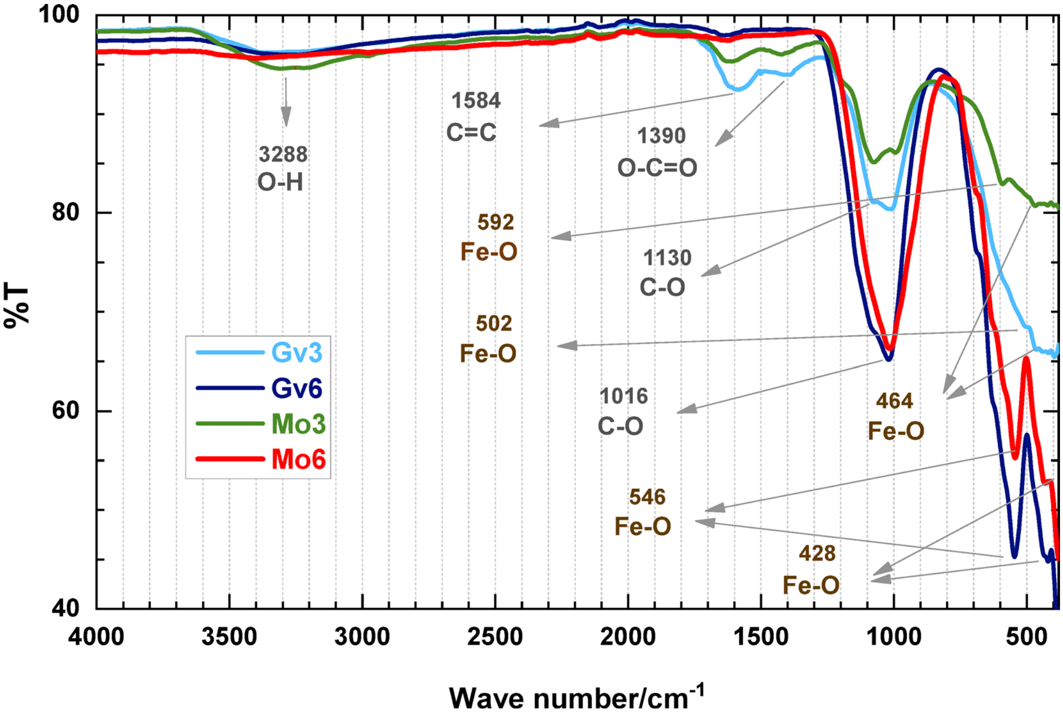

Fig. 7. FTIR spectra of iron oxide nanoparticles (magnetite and hematite) synthesized using Guava (Gv) and Moringa (Mo) leaf extracts, calcined at 300 °C (Gv3, Mo3) and 600 °C (Gv6, Mo6).

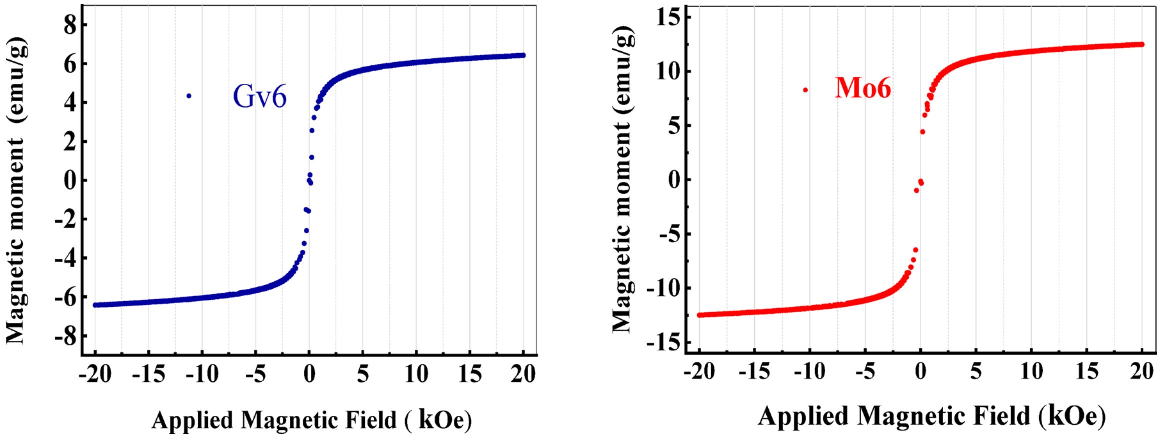

Fig. 8. VSM hysteresis loops of iron oxide nanoparticles (magnetite and hematite) synthesized using Guava (Gv6) and Moringa (Mo6) leaf extracts, calcined at 600 °C, showing magnetic moment versus applied magnetic field (± 20 kOe) measured at room temperature.

clear superparamagnetic behavior, as evidenced by S-shaped hysteresis loops with negligible coercivity and remanence. Mo6 displays a saturation magnetization (Ms) of approximately 13 emu/g, while Gv6 shows a lower Ms of around 6 emu/g. These values fall below the typical range reported for Fe_3O_4 nanoparticles in the recent studies of Laurent et al.[90]. and Wu et al.[91]. However, both values are consistent with reports in the literature for small or coated iron oxide nanoparticles. For instance, Thanh et al.[92]. and Lee et al.[93]. observed saturation magnetization values (Ms) ranging from 5 to 25 emu/g for nanoparticles smaller than 8 nm. According to these reports, reduced Ms is common in nanoparticles due to small size, high surface disorder, or organic coatings. Additionally, the presence of hematite nanoparticles alongside magnetite likely contributes to the lower Ms values compared to pure magnetite nanoparticles[83]. Such superparamagnetic nature and low remanence of both samples are typical of nanoparticles designed for biomedical use, such as in MRI and drug delivery, where minimizing particle aggregation is essential to ensure safety[90,94].

Antibacterial and photocatalytic activities

The antibacterial activity of the synthesized iron oxide nanoparticles against *Escherichia coli* (*E. coli*) was tested under both light and dark conditions[95,96]. Prior to the experiment, all equipment and the nutrient agar medium (prepared by dissolving 1 g of nutrient agar in 100 mL of water) were sterilized by autoclaving at 120 °C and 3 atm pressure for 30 min, followed by UV radiation treatment. After cooling the agar solution to 50 °C, 10 mL aliquots were poured into sterile Petri dishes and allowed to solidify.

For the antibacterial assay, 1.5 mg of the synthesized iron oxide nanoparticles was dispersed in 5 mL of deionized water by sonication for 5 min to ensure a uniform suspension. To this, 250 µL of *E. coli* bacterial culture with a concentration of 1.5 × 10^8 CFU/mL was added. The resulting mixtures were then divided into two groups: one exposed to tungsten lamp irradiation for 1 h to assess photocatalytic activity, and the other kept in the dark for the same duration as a control.

After treatment, each suspension was diluted to a total volume of 16 mL by adding 10.75 mL of distilled water, followed by a 30-fold serial dilution. From these diluted samples, 10 µL aliquots were spread evenly onto the prepared agar plates, which were incubated at 37 °C for 24 h to allow bacterial colony formation. A control without nanoparticles was also included for comparison. Following incubation, the bacterial colonies were counted using the plate colony counting method. Representative images of the Petri dishes are presented in Fig. 9 to illustrate the antibacterial and photocatalytic effects of the nanoparticles.

When comparing bacterial growth on plates incubated under both dark and light conditions, a noticeable inhibitory effect of the nanoparticles was observed. In all cases, the colony-forming units (CFU) on plates treated with nanoparticles were lower than those with the control solutions. In the dark, CFU counts for the control solutions was 998, whereas for solutions with samples Gv3, Gv6, Mo3, and Mo6, they were found to be 562, 712, 908, and 740, respectively. Upon light exposure, these counts decreased to 729 for the control solution and to 337, 466, 511, and 364, respectively, for the solutions with the same samples. Figure 10 illustrates the comparison of *E. coli* colonies in the presence of these samples under light versus dark conditions, showing that light exposure enhances bacterial growth inhibition.

For Gv3 and Gv6, the reduction in CFU under light compared to dark conditions was comparable to that observed in the control solutions, suggesting minimal photocatalytic contribution. Conversely, Mo3 and Mo6 exhibited noticeably lower CFU under light exposure relative to dark conditions, indicating pronounced photocatalytic antibacterial activity. This observation is consistent with the UV-vis spectral analysis (Fig. 6), which showed sharp absorption peaks and favorable band gaps (1.52–4.78 eV) for Mo3 and Mo6, indicating efficient light absorption and photocatalytic reactive oxygen species (ROS) generation.

Detailed studies on antibacterial activity, its underlying mechanisms, and cytotoxicity to human cells can confirm the biocompatibility and safety of such nanoparticles. Several research reports offer valuable insights in this regard[97–107]. Ezealigo et al.[97] emphasized in their report that IONPs are promising antibacterial agents due to their ROS-mediated mechanisms. S.V. Gudkov et al.[98]. in their comprehensive review, summarized multiple studies demonstrating the antimicrobial effects of IONPs. In these reports, two primary antibacterial mechanisms of IONPs were emphasized: (1) generation of ROS, which induces oxidative damage to bacterial cells, and (2) membrane disruption, whereby IONPs physically damage bacterial membranes. Singh et al.[99] noted that the primary antibacterial action of IONPs involves ROS generation, which causes oxidative damage to bacterial cells by disrupting membranes, damaging DNA, and inhibiting key enzymes. IONPs can also directly damage bacterial cell membranes, increasing permeability and causing leakage of cellular contents that leads to bacterial death. While the precise antibacterial mechanisms of iron oxide nanoparticles can be multifaceted, our data primarily support a photocatalytic ROS-mediated mechanism for the synthesized IONPs Mo3 and Mo6 under light exposure. As illustrated in Fig. 11, the antibacterial effect under light is likely mediated by photocatalytically generated ROS, such as hydroxyl radicals ($^{*}OH$) and superoxide anions ($^{*}O_2^{-}$), which induce oxidative damage to bacterial cell membranes, ultimately leading to cell death[103,104]. For Gv3 and Gv6, the mechanism appears

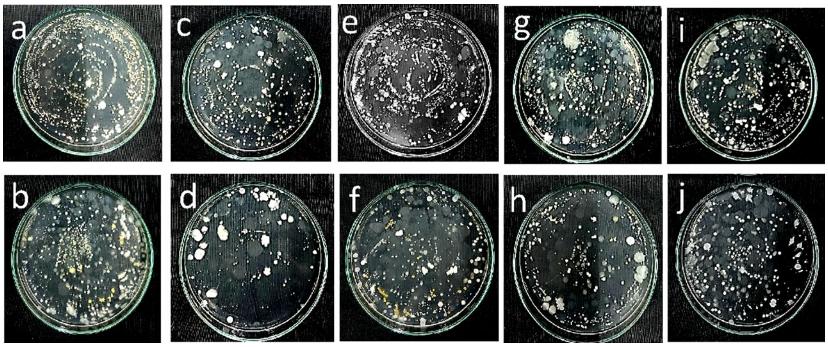

Fig. 9. Photographs of *E. coli* colony forming units (CFU) grown on agar plates for the blank solution and solutions containing iron oxide nanoparticles (magnetite and hematite) synthesized using Guava (Gv) and Moringa (Mo) leaf extracts. Panels (**a**, **c**, **e**, **g**, **i**) show plates incubated in the dark, and panels (**b**, **d**, **f**, **h**, **j**) show plates incubated under light for the blank solution and for solutions with Gv3, Gv6, Mo3, and Mo6 respectively. Here, Gv3 and Mo3 are nanoparticles calcined at 300 °C, while Gv6 and Mo6 are nanoparticles calcined at 600 °C.

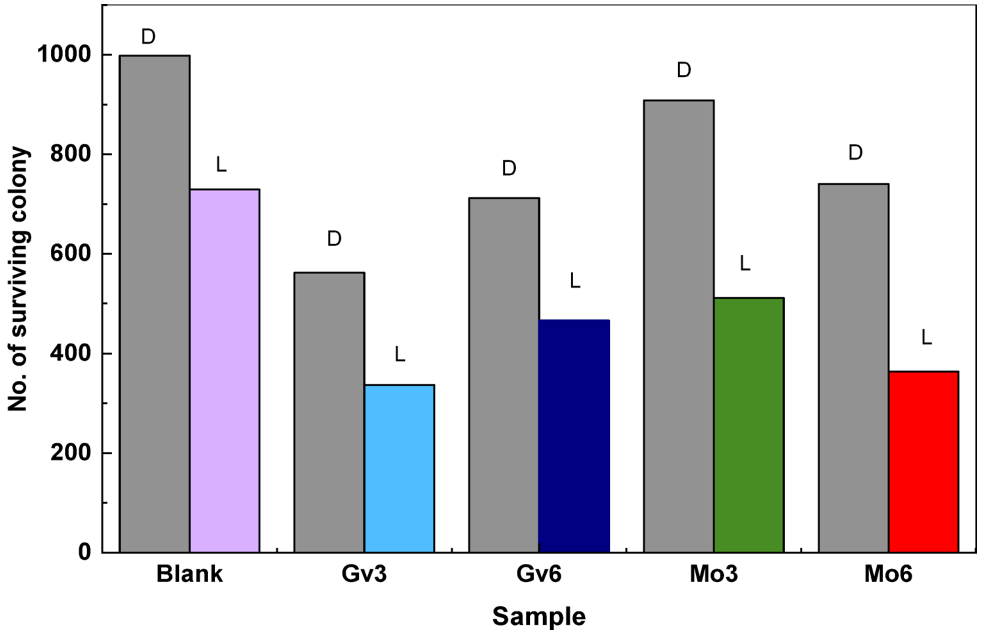

Fig. 10. Comparison of *E. coli* colony counts under dark (D) and light (L) exposure in blank solution and solutions containing iron oxide nanoparticles (magnetite and hematite) synthesized using Guava (Gv) and Moringa leaf (Mo) extracts, calcined at 300 °C (Gv3, Mo3) and 600 °C (Gv6, Mo6).

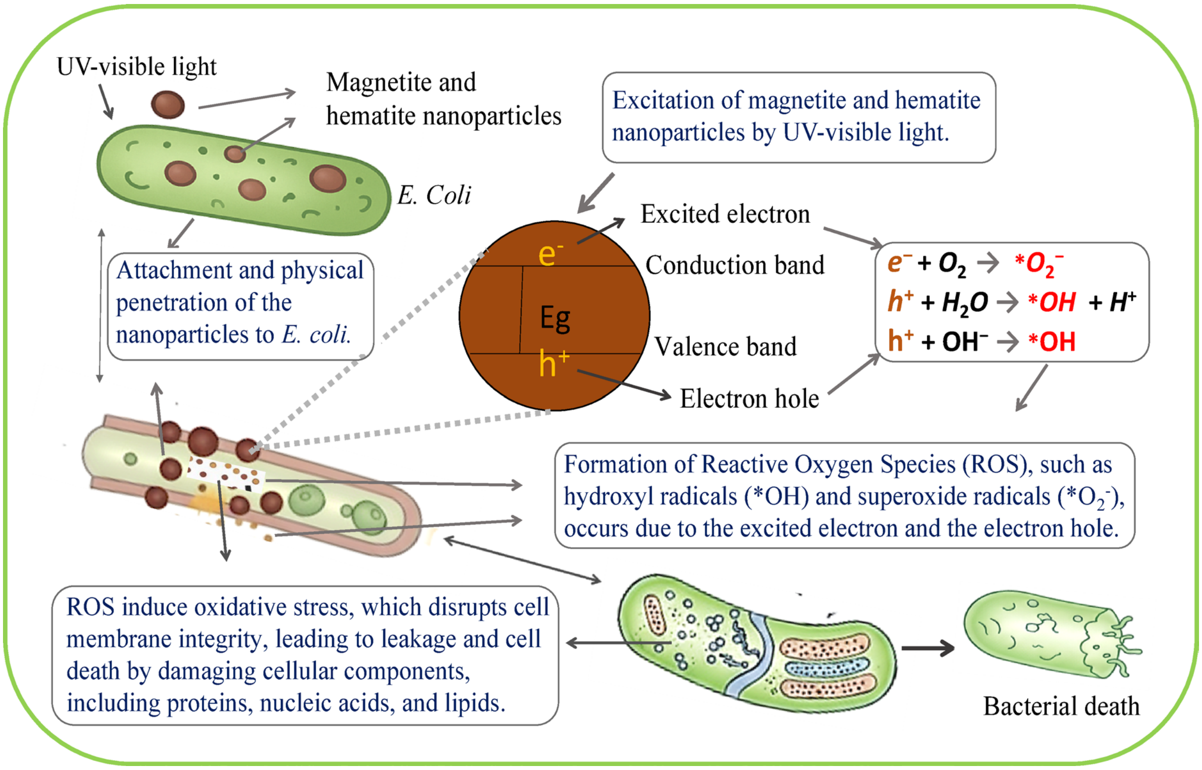

$e^- + O_2 \rightarrow {}^*O_2^-$

$h^+ + H_2O \rightarrow {}^*OH + H^+$

$h^+ + OH^- \rightarrow {}^*OH$

Formation of Reactive Oxygen Species (ROS), such as hydroxyl radicals (*OH) and superoxide radicals (*O_2^-), occurs due to the excited electron and the electron hole.

ROS induce oxidative stress, which disrupts cell membrane integrity, leading to leakage and cell death by damaging cellular components, including proteins, nucleic acids, and lipids.

Fig. 11. Antibacterial activity of green synthesized iron oxide nanoparticles (magnetite and hematite) against *E. coli*, showing growth inhibition and membrane disruption via ROS generated by electron-hole pairs formed upon UV-visible light absorption.

less dependent on light activation and may involve other nanoparticle–bacteria interactions which require further investigation. Although concerns exist regarding the toxicity of iron oxide nanoparticles to human cells, multiple studies[98–100] demonstrated that their cytotoxic effects depend on several factors, including particle size, concentration, and exposure duration. Additionally, surface coatings often enhance biocompatibility and help reduce toxicity[100]. Previous reports by Gudkov et al.[98]. and Kiroriwal et al.[100] demonstrated that iron oxide nanoparticles exhibit significant antibacterial activity with relatively low cytotoxicity, suggesting their potential for biomedical applications. In this context, we propose that our synthesized nanoparticles, specifically Mo3 and Mo6 coated with biomolecules from Moringa extract, may serve as effective antibacterial agents.

Conclusion

In conclusion, this study demonstrates a simple and sustainable green approach for synthesizing superparamagnetic magnetite and hematite nanoparticles in the size range of 20 to 30 nm. It ensures a fully green protocol and overcomes common challenges in producing the targeted nanoparticles by integrating key factors. These include the use of widely available *Moringa oleifera* and *Psidium guajava* leaf extracts with a favorable composition of biomolecules and pH, an environmentally benign precursor salt at an optimal concentration, the elimination of hazardous chemicals for pH adjustment, and a unique calcination strategy. Characterization techniques including UV–vis, XRD, FTIR, FESEM, and VSM confirmed the formation of the targeted amorphous and crystalline nanoparticles, exhibiting superparamagnetic behavior. Moringa-derived particles showed a higher saturation magnetization (~ 13 emu/g) compared to Guava-derived particles (~ 6 emu/g). FTIR analysis confirmed Fe–O bond formation and bio-organic surface capping on the nanoparticle surfaces. Preliminary antibacterial tests showed moderate activity against *Escherichia coli*, which improved under light irradiation, indicating the nanoparticles' potential photocatalytic properties. Their superparamagnetic nature and tunable band gap make them promising for biomedical applications, energy harvesting, and catalysis. While further analyses, including TEM, Raman spectroscopy, stability testing, BET surface area measurements, and detailed antibacterial or cytotoxicity studies are necessary to gain deeper insights and validate safety, these are planned for future work due to current facility limitations. Overall, this synthesis approach provides a robust, scalable, and eco-friendly platform for producing low-cost, well-defined, superparamagnetic magnetite and hematite nanoparticles, facilitating their application in environmental remediation, biomedical fields, and energy technologies, advancing sustainable development goals.

Data availability

Raw data obtained during analysis in this study are included in Supplementary Information files.

Received: 25 October 2024; Accepted: 22 September 2025

References

1. Wang, H., Liang, X., Wang, J., Jiao, S. & Xue, D. Multifunctional inorganic nanomaterials for energy applications. *Nanoscale* **12**, 14–42 (2020).
2. Ong, W. J., Zheng, N. & Antonietti, M. Advanced nanomaterials for energy conversion and storage: current status and future opportunities. *Nanoscale* **13**, 9904–9907 (2021).
3. Zhang, Q., Uchaker, E., Candelaria, S. L. & Cao, G. Nanomaterials for energy conversion and storage. *Chem. Soc. Rev.* **42**, 3127–3171 (2013).
4. Nor Fatina, R., Norazuwana, S., Siti, K., Mohd Shabudin, M. & Rozan, M. Y. An overview of nanomaterials in fuel cells: synthesis method and application. *Int. J. Hydrogen Energy*. **47**, 18468–18495 (2022).
5. Murali, A., Lokhande, G., Deo, K. A., Brokesh, A. & Gaharwar, A. K. Emerging 2D nanomaterials for biomedical applications. *Mater. Today*. **50**, 276–302 (2021).
6. Das, S., Sen, B. & Debnath, N. Recent trends in nanomaterials applications in environmental monitoring and remediation. *Environ. Sci. Pollut Res.* **22**, 18333–18344 (2015).
7. Roy, A., Sharma, A., Yadav, S., Jule, L. T. & Krishnaraj, R. Nanomaterials for remediation of environmental pollutants. *Bioinorg Chem. Appl.* 1764647 (2021).
8. Ray, P. C. Size and shape dependent second order nonlinear optical properties of nanomaterials and their application in biological and chemical sensing. *Chem. Rev.* **110**, 5332–5365 (2010).
9. Baig, N., Kammakakam, I. & Falath, W. Nanomaterials: a review of synthesis methods, properties, recent progress, and challenges. *Mater. Adv.* **2**, 1821–1871 (2021).
10. Karami, H. Heavy metal removal from water by magnetite nanorods. *Chem. Eng. J.* **219**, 209–216 (2013).
11. Baumgartner, J., Bertinetti, L., Widdrat, M., Hirt, A. M. & Faivre, D. Formation of magnetite nanoparticles at low temperature: from superparamagnetic to stable single domain particles. *PloS One*. **8**, e57070 (2013).
12. Maharjan, A., Dikshit, P. K., Gupta, A. & Kim, B. S. Catalytic activity of magnetic iron oxide nanoparticles for hydrogen peroxide decomposition: optimization and characterization. *J. Chem. Technol. Biotechnol.* **95**, 2495–2508 (2020).
13. Groiss, S., Selvaraj, R., Varadavenkatesan, T. & Vinayagam, R. Structural characterization, antibacterial and catalytic effect of iron oxide nanoparticles synthesised using the leaf extract of *Cynometra Ramiflora*. *J. Mol. Struct.* **1128**, 572–578 (2017).
14. Vaseem, M., Ghaffar, F. A., Farooqui, M. F. & Shamim, A. Iron oxide nanoparticle-based magnetic ink development for fully printed tunable radio-frequency devices. *Adv. Mater. Technol.* **3**, 1700242 (2018).
15. Qureshi, A. A. et al. Systematic investigation of structural, morphological, thermal, optoelectronic, and magnetic properties of high-purity hematite/magnetite nanoparticles for optoelectronics. *Nanomaterials* **12**, 1635 (2022).
16. Asha, A., Chamundeeswari, M., Flora, R. M. N. & Preethy, K. R. Optimization of hematite nanoparticles from natural ore as novel imaging agents: a green chemistry approach. *Biotechnol Appl. Biochem* **71**(4), 791–808 (2024).
17. Kumar, S. et al. Electrochemical paper based cancer biosensor using iron oxide nanoparticles decorated PEDOT: PSS. *Anal. Chim. Acta*. **1056**, 135–145 (2019).
18. Jabbar, K. Q., Barzinjy, A. A. & Hamad, S. M. Iron oxide nanoparticles: Preparation methods, functions, adsorption and coagulation/flocculation in wastewater treatment. *Environ. Nanotechnol Monit. Manage.* **17**, 100661 (2022).
19. Sangaiya, P. & Jayaprakash, R. A review on iron oxide nanoparticles and their biomedical applications. *J. Supercond. Novel Magn.* **31**, 3397–3413 (2018).

20. Vangijzegem, T., Stanicki, D. & Laurent, S. Magnetic iron oxide nanoparticles for drug delivery: applications and characteristics. *Expert Opin. Drug Deliv*. **16**, 69–78 (2019).
21. Abenojar, E. C., Wickramasinghe, S., Bas-Concepcion, J. & Samia, A. C. Structural effects on the magnetic hyperthermia properties of iron oxide nanoparticles. *Prog Nat. Sci. : Mater. Int.* **26**, 440–448 (2016).
22. Tasnim, N. T., Ferdous, N., Rumon, M. M. H. & Shakil, M. S. The promise of metal-doped iron oxide nanoparticles as antimicrobial agent. *ACS Omega*. **9**, 16–32 (2023).
23. Marcinowski, P. et al. Magnetite and hematite in advanced oxidation processes application for cosmetic wastewater treatment. *Processes* **8**, 1343 (2020).
24. Saied, E. et al. Mycosynthesis of hematite (α-Fe_2O_3) nanoparticles using Aspergillus Niger and their antimicrobial and photocatalytic activities. *Bioengineering* **9**, 397 (2022).
25. Miri, A., Khatami, M. & Sarani, M. Biosynthesis, magnetic and cytotoxic studies of hematite nanoparticles. *J. Inorg. Organomet. Polym. Mater.* **30**, 767–774 (2020).
26. Asha, A. B. & Narain, R. Nanomaterials properties. *Polymer Sci. Nanotechnology* 343–359 (2020).
27. Abid, N. et al. Synthesis of nanomaterials using various top-down and bottom-up approaches, influencing factors, advantages, and disadvantages: a review. *Adv. Colloid Interface Sci.* **300**, 102597 (2022).
28. Jamkhande, P. G., Ghule, N. W., Bamer, A. H. & Kalaskar, M. G. Metal nanoparticles synthesis: an overview on methods of preparation, advantages and disadvantages, and applications. *J. Drug Deliv Sci. Technol.* **53**, 101174 (2019).
29. Jana, N. R., Gearheart, L. & Murphy, C. J. Seeding growth for size control of 5 – 40 Nm diameter gold nanoparticles. *Langmuir* **17**, 6782–6786 (2001).
30. Zhang, Y., Poon, K., Masonsong, G. S. P., Ramaswamy, Y. & Singh, G. Sustainable nanomaterials for biomedical applications. *Pharmaceutics* **15**, 922 (2023).
31. Parveen, K., Banse, V. & Ledwani, L. Green synthesis of nanoparticles: their advantages and disadvantages. In *AIP Conf. Proc.*AIP Publishing, (2016).
32. Salem, S. S. & Fouda, A. Green synthesis of metallic nanoparticles and their prospective biotechnological applications: an overview. *Biol. Trace Elem. Res.* **199**, 344–370 (2021).
33. Sharma, D., Kanchi, S. & Bisetty, K. Biogenic synthesis of nanoparticles: a review. *Arab. J. Chem.* **12**, 3576–3600 (2019).
34. Altemimi, A., Lakhssassi, N., Baharlouei, A., Watson, D. G. & Lightfoot, D. A. Phytochemicals: Extraction, isolation, and identification of bioactive compounds from plant extracts. *Plants* **6**, 42 (2017).
35. Monagas, M. et al. Understanding plant to extract ratios in botanical extracts. *Front. Pharmacol.* **13**, 981978 (2022).
36. Kanagasubbulakshmi, S. & Kadirvelu, K. Green synthesis of iron oxide nanoparticles using lagenaria siceraria and evaluation of its antimicrobial activity. *Def. Life Sci. J.* **2**, 422–427 (2017).
37. Buarki, F., AbuHassan, H., Hannan, A. & Henari, F. F. Green synthesis of iron oxide nanoparticles using *Hibiscus rosa sinensis* flowers and their antibacterial activity. *J. Nanotechnol.* **2022**, 5474645, (2022).
38. Karpagavinayagam, P. & Vedhi, C. Green synthesis of iron oxide nanoparticles using *Avicennia Marina* flower extract. *Vacuum* **160**, 286–292 (2019).
39. Demirezen, D. A., Yıldız, Y. Ş., Yılmaz, Ş. & Yılmaz, D. D. Green synthesis and characterization of iron oxide nanoparticles using *Ficus carica* (common fig) dried fruit extract. *J. Biosci. Bioeng.* **127**, 241–245 (2019).
40. Niraimathee, V., Subha, V., Ravindran, R. E. & Renganathan, S. Green synthesis of iron oxide nanoparticles from *Mimosa pudica* root extract. *Int. J. Environ. Sustain. Dev.* **15**, 227–240 (2016).
41. Jamzad, M. & Kamari Bidkorpeh, M. Green synthesis of iron oxide nanoparticles by the aqueous extract of *Laurus nobilis* L. leaves and evaluation of the antimicrobial activity. *J. Nanostruct. Chem.* **10**, 193–201 (2020).
42. Lakshminarayanan, S., Shereen, M. F., Niraimathi, K., Brindha, P. & Arumugam, A. One-pot green synthesis of iron oxide nanoparticles from bauhinia tomentosa: characterization and application towards synthesis of 1, 3 diolein. *Sci. Rep.* **11**, 8643 (2021).
43. El-Seedi, H. R. et al. Updated review of metal nanoparticles fabricated by green chemistry using natural extracts: Biosynthesis, Mechanisms, and applications. *Bioeng. (Basel)*. **11**, 1095 (2024).
44. Priya, P., Sidhu, A. K., Naveen, N. & Kaur, K. Green synthesis: an eco-friendly route for the synthesis of iron oxide nanoparticles. *Front. Nanotechnol.* **3**, 655062 (2021).
45. Perumalsamy, H. et al. A comprehensive review on Moringa Oleifera nanoparticles: importance of polyphenols in nanoparticle synthesis, nanoparticle efficacy and their applications. *J. Nanobiotechnol.* **22**, 71 (2024).
46. Raza, F., Azad, A., Zafar, H. & Sulaiman, M. Factors influencing the green synthesis of metallic nanoparticles using plant extracts: a comprehensive review. *Pharm Fronts* **5**, e117–e131 (2023).
47. Bouttier-Figueroa, D. C., Cortez-Valadez, J. M., Flores-Acosta, M. & Robles-Zepeda, R. E. Synthesis of metallic nanoparticles using plant's natural extracts: synthesis mechanisms and applications. *Biotecnia* **25**, 125–139 (2023).
48. Shahzadi, S., Fatima, S., Ul Ain, Q., Shafiq, Z. & Janjua, M. R. S. A. A review on green synthesis of silver nanoparticles (SNPs) using plant extracts: a multifaceted approach in photocatalysis, environmental remediation, and biomedicine. *RSC Adv.* **15**, 3858–3903 (2025).
49. Nagajyothi, P. C., Shim, J., Pandurangan, M., Kim, D. H. & Sreekanth, T. V. M. Green synthesis of iron oxide nanoparticles and their catalytic and in vitro anticancer activities. *J Cluster Sci.* **28**, 245–257 (2016).
50. Thacker, H., Ram, V. & Dave, P. Plant mediated synthesis of iron nanoparticles and their applications: a review. *Prog Chem. Biochem. Res.* **2**, 84–91 (2019).
51. Ebrahiminezhad, A. et al. Plant-mediated synthesis and applications of iron nanoparticles. *Mol. Biotechnol.* **60**, 154–168 (2018).
52. Abdullah, J. A. A. et al. Sustainable nanomagnetism: investigating the influence of green synthesis and pH on iron oxide nanoparticles for enhanced biomedical applications. *Polymers* **15**, 3850 (2023).
53. Yadwade, R., Ankamwar, B. & Kirtiwar, S. A review on green synthesis and applications of iron oxide nanoparticles. *J. Nanosci. Nanotechnol.* **21**, 5812–5834 (2021).
54. Khan, F. et al. Green nanotechnology: plant-mediated nanoparticle synthesis and application. *Nanomaterials (Basel)*. **12**, 673 (2022).
55. Shabbir, M. A. et al. Synthesis of iron oxide nanoparticles from Madhuca indica plant extract and assessment of their cytotoxic, antioxidant, anti-inflammatory, and anti-diabetic properties via different nanoinformatics approaches. *ACS Omega*. **8**, 33358–33366 (2023).
56. Kulkarni, S., Mohanty, N., Kadam, N. N., Swain, N. & Thakur, M. Green synthesis to develop iron-nano formulations and its toxicity assays. *J. Pharmacopunct.* **23**, 165–172 (2020).
57. Mohamed, A. et al. Green synthesis and characterization of iron oxide nanoparticles for the removal of heavy metals (Cd^{2+} and Ni^{2+}) from aqueous solutions with antimicrobial investigation. *Sci. Rep.* **13**, 7227 (2023).
58. Üstün, E., Önbaş, S. C., Çelik, S. K., Ayvaz, M. Ç. & Şahin, N. Green synthesis of iron oxide nanoparticles by using *Ficus carica* leaf extract and its antioxidant activity. *Biointerface Res. Appl. Chem.* **12**, 2108–2116 (2022).
59. Razack, S. A. et al. Green synthesis of iron oxide nanoparticles using hibiscus rosa-sinensis for fortifying wheat biscuits. *SN Appl. Sci.* **2**, 5 (2020).
60. Al-Karagoly, H. et al. Green synthesis, characterization, cytotoxicity, and antimicrobial activity of iron oxide nanoparticles using Nigella sativa seed extract. *Green. Process. Synth.* **11**, 254–265 (2022).

61. Devi, H. S., Wani, A. H., Parveen, S., Shah, M. A. & Boda, M. A. Green synthesis of iron oxide nanoparticles using Platanus orientalis leaf extract for antifungal activity. *Green. Process. Synth.* **8**, 38–45 (2018).
62. Bhuiyan, M. S. H. et al. Green synthesis of iron oxide nanoparticle using carica Papaya leaf extract: application for photocatalytic degradation of remazol yellow RR dye and antibacterial activity. *Heliyon* **6**, e04603 (2020).
63. Thatyana, M. et al. Advances in phytonanotechnology: a plant-mediated green synthesis of metal nanoparticles using phyllanthus plant extracts and their antimicrobial and anticancer applications. *Nanomaterials* **13**, 2616 (2023).
64. Khan, F. et al. Green nanotechnology: plant-mediated nanoparticle synthesis and application. *Nanomaterials* **12**, 673 (2022).
65. Braham, F. et al. Online HPLC-DPPH screening method for evaluation of radical scavenging phenols extracted from Moringa Oleifera leaves. *S Afr. J. Bot.* **129**, 146–154 (2019).
66. Oladeji, O. S., Odelade, K. A. & Oloke, J. K. Phytochemical screening and antimicrobial investigation of Moringa Oleifera leaf extracts. *Afr. J. Sci. Technol. Innov. Dev.* **12**, 79–84 (2019).
67. Chatzimitakos, T. et al. Optimization of pressurized liquid extraction (PLE) parameters for extraction of bioactive compounds from Moringa Oleifera leaves and bioactivity assessment. *Int. J. Mol. Sci.* **25**, 4628 (2024).
68. Islam, M. J. et al. Psidium Guajava leaf extract mediated green synthesis of silver nanoparticles and its application in antibacterial coatings. *RSC Adv.* **13**, 19164–19172 (2023).
69. Kumar, M. et al. Guava (Psidium Guajava L.) leaves: nutritional composition, phytochemical profile, and health-promoting bioactivities. *Foods* **10**, 752 (2021).
70. Ruksiriwanich, W. et al. Guava (Psidium Guajava L.) leaf extract as bioactive substances for anti-androgen and antioxidant activities. *Plants* **11**, 3514 (2022).
71. Görke, M., Okeil, S., Menzel, D., Semenenko, B. & Garnweitner, G. Tuning the properties of iron oxide nanoparticles in thermal decomposition synthesis: A comparative study of the influence of temperature, ligand length and ligand concentration. *Part. Part. Syst. Charact.* **41** (10), 2400059 (2024).
72. Gatta, G. D., Kantor, I., Ballaran, B., Dubrovinsky, T., McCammon, C. & L. & Effect of non-hydrostatic conditions on the elastic behaviour of magnetite: an in situ single-crystal X-ray diffraction study. *Phys. Chem. Min.* **34**, 627–635 (2007).
73. Yu, S. C., Lee, J. S., Tung, S. F. & Lan, C. L. *J. Geol. Soc. China* **42**, 349, (1999).
74. Balu, P., Asharani, I. & Thirumalai, D. Catalytic degradation of hazardous textile dyes by iron oxide nanoparticles prepared from *Raphanus sativus* leaves' extract: a greener approach. *J. Mater. Sci. : Mater. Electron.* **31**, 10669–10676 (2020).
75. Bouafia, A., Laouini, S. E., Khelef, A., Tedjani, M. L. & Guemari, F. Effect of ferric chloride concentration on the type of magnetite (Fe_3O_4) nanoparticles biosynthesized by aqueous leaves extract of *Artemisia* and assessment of their antioxidant activities. *J. Cluster Sci.* **32**, 1033–1041 (2021).
76. Akbar, A. Q. et al. Systematic investigation of Structural, Morphological, Thermal, Optoelectronic, and magnetic properties of High-Purity Hematite/Magnetite nanoparticles for optoelectronics. *Nanomaterials*, **12**,1635, (2022).
77. Mohammed, M. & Hawar, S. N. G. M. Green biosynthesis of silver nanoparticles from *Moringa oleifera* leaves and its antimicrobial and cytotoxicity activities. *Int. J. Biomater.* **2022**, 4136641 (2022).
78. Somchaidee, P. & Tedsree, K. Green synthesis of high dispersion and narrow size distribution of zero-valent iron nanoparticles using guava leaf (*Psidium Guajava* L) extract. *Adv. Nat. Sci. : Nanosci. Nanotechnol.* **9**, 035006 (2018).
79. Indrayana, I. P. T. Synthesis, characterization, and application of Fe3O4 nanoparticles as a signal amplifier element in surface plasmon resonance biosensing. *J. Online Phys.* **5**, 65–74 (2020).
80. Saadati, M., Akhavan, O. & Fazli, H. Single-layer MoS_2-MoO_3-x heterojunction nanosheets with simultaneous photoluminescence and co-photocatalytic features. *Catalysts* **11**, 1445 (2021).
81. Mohammad Hosseini, N., Sheshmani, S., Shahvelayati, A. S., Ahmadi, R. & Adhami, F. Development and characterization of environmentally-friendly magnetically graphene oxide-embedded Chitosan as a recyclable heterogeneous photocatalyst. *J. Polym. Environ.* **32**, 1952–1971 (2024).
82. Muthukumar, B. et al. Synthesis and characterization of iron oxide nanoparticles from lawsonia inermis and its effect on the biodegradation of crude oil hydrocarbon. *Sci. Rep.* **14**, 11335 (2024).
83. Srivastava, N. et al. Sustainable green approach to synthesize Fe_3O_4/α-Fe_2O_3 nanocomposite using waste pulp of syzygium cumini and its application in functional stability of microbial cellulases. *Sci. Rep.* **11**, 24371 (2021).
84. Nag, S., Roychowdhury, A., Das, D. & Mukherjee, S. Synthesis of α-Fe_2O_3-functionalised graphene oxide nanocomposite by a facile low temperature method and study of its magnetic and hyperfine properties. *Mater. Res. Bull.* **74**, 109–116 (2016).
85. Kumar, V., Yadav, S. K. & Yadav, S. C. Green synthesis of silver nanoparticles using polyphenolic compounds: characterization and antimicrobial activity. *J. Nanomed. Nanotechnol.* **6**, 1–7 (2015).
86. Socrates, G. Infrared and raman characteristic group frequencies*: Tables and Charts* 3rd edn (Wiley, 2001).
87. Pavia, D. L., Lampman, G. M., Kriz, G. S. & Vyvyan, J. R. *Introduction To Spectroscopy* 5th edn (Cengage Learning, 2014).
88. Nakamoto, K. Infrared and raman spectra of inorganic and coordination compounds 6th edn (Wiley, 2009).
89. Silverstein, R. M., Webster, F. X. & Kiemle, D. J. Spectrometric identification of organic compounds 7th edn (Wiley, 2005).
90. Laurent, S., Dutz, S., Häfeli, U. O. & Mahmoudi, M. Magnetic fluid hyperthermia: focus on superparamagnetic iron oxide nanoparticles. *Chem. Rev.* **124**, 311–356 (2024).
91. Wu, K., Su, D., Saha, R., Liu, J. & Wang, J. P. Magnetic nanoparticles: synthesis, surface modifications and applications in diagnosis and therapy. *J. Magn. Magn. Mater.* **593**, 170838 (2024).
92. Thanh, N. T. K., Maclean, N. & Mahiddine, S. Mechanisms of nucleation and growth of nanoparticles in solution. *Nat. Rev. Chem.* **7**, 278–294 (2023).
93. Lee, J. H. et al. Artificially engineered magnetic nanoparticles for ultra-sensitive molecular imaging. *Adv. Funct. Mater.* **34**, 2401234 (2024).
94. Li, X., Zhang, Y., Wang, X., Xu, Y. & Chen, Y. Surface engineering of iron oxide nanoparticles for biomedical applications. *ACS Appl. Nano Mater.* **6**, 12345–12356 (2023).
95. Olsen, R. A. & Bakken, L. R. Viability of soil bacteria: optimization of plate-counting technique and comparison between total counts and plate counts within different size groups. *Microb. Ecol.* **13**, 59–74 (1987).
96. Pan, H., Zhang, Y., He, G. X., Katagori, N. & Chen, H. A comparison of conventional methods for the quantification of bacterial cells after exposure to metal oxide nanoparticles. *BMC Microbiol.* **14**, 222 (2014).
97. Ezealigo, U. S., Ezema, F. I., Aisida, S. O. & Ezealigo, B. N. Iron oxide nanoparticles in biological systems: antibacterial and toxicology perspective. *JCIS Open.* **4**, 100027 (2021).
98. Gudkov, S. V. et al. Do iron oxide nanoparticles have significant antibacterial properties? *Antibiotics* **10**, 884 (2021).
99. Singh, R. et al. Iron oxide nanoparticles in biological systems: antibacterial and cytotoxic effects. *Mater. Today Commun.* **29**, 102864 (2021).
100. Kiroriwal, M. et al. Iron oxide nanoparticles: antibacterial and cytotoxic Activity—A systematic review. *Sens. Lett.* **18**, 596–604 (2020). Hernandez-Ramirez, J., Rodriguez-Lopez, J. L. & Hernandez-Guerrero, J.
101. Gabrielyan, L., Badalyan, H., Gevorgyan, V. & Trchounian, A. Comparable antibacterial effects and action mechanisms of silver and iron oxide nanoparticles on *Escherichia coli* and *Salmonella typhimurium*. *Sci. Rep.* **10**, 13145 (2020).
102. Batool, F. et al. Biologically synthesized iron nanoparticles (FeNPs) from *Phoenix dactylifera* have anti-bacterial activities. *Sci. Rep.* **11**, 22132 (2021).
103. Mendes, C. R. et al. Antibacterial action and target mechanisms of zinc oxide nanoparticles against bacterial pathogens. *Sci. Rep.* **12**, 2658 (2022).

104. Schoenhalz, A. L., Arantes, J. T., Fazzio, A. & Dalpian, G. M. Surface and quantum confinement effects in ZnO nanocrystals. *J. Phys. Chem. C.* **114**, 18293–18297 (2010).
105. Hossain, M. A. et al. Synthesis of Fe- or Ag-doped TiO2–MWCNT nanocomposite thin films and their visible-light-induced catalysis of dye degradation and antibacterial activity. *Res. Chem. Intermed.* **44**, 2667–2683 (2018).
106. Maness, P. C. et al. Bactericidal activity of photocatalytic TiO2 reaction: toward an Understanding of its killing mechanism. *Appl. Environ. Microbiol.* **65**, 4094–4098 (1999).
107. Siddiqui, M. A. et al. Iron oxide nanoparticles induced cytotoxicity, oxidative stress, cell cycle arrest, and DNA damage in human Um bilical vein endothelial cells. *J. Trace Elem. Med. Biol.* **80**, 127302 (2023).

Acknowledgements

The authors gratefully acknowledge the financial support from the Research and Publication Cell, University of Chittagong, Bangladesh, through the research grant for the project entitled "Synthesis of Metal Oxide Nanoparticles by Two Different Approaches and Their Characterization."

Author contributions

S. K. B. designed the research project, supervised the research, analyzed samples and results, and prepared, reviewed, and edited the manuscript; D. S. performed laboratory work on the original synthesis by Mo; N. H. participated in laboratory work on synthesis by Mo and Gv, and calculated nanoparticle size; M. J. (A) contributed to collecting relevant information from the literature and preparing the manuscript; J. F. participated in the synthesis process and analyzed samples; U. J. (B) N. collected literature data through background study and contributed to preparing a part of the initial draft; K. F. collected literature data through background study and contributed to preparing a part of the initial draft; R. J. S. participated in the synthesis process by Mo; R. J. (C) reviewed the manuscript and edited the final draft; P. C. performed the antibacterial and photocatalytic activity experiments and prepared the initial draft for that section; M. N. U. supervised the antibacterial and photocatalytic activity experiments and contributed to analyzing the observations for that section.

Declarations

Competing interests

The authors declare no competing interests.

Additional information

Supplementary Information The online version contains supplementary material available at https://doi.org/10.1038/s41598-025-21603-4.

Correspondence and requests for materials should be addressed to S.K.B.

Reprints and permissions information is available at www.nature.com/reprints.